Fuel 289 (2021) 119776

Contents lists available at ScienceDirect

Fuel

journal homepage: www.elsevier.com/locate/fuel

Full Length Article

# Effects of precursor concentration on morphologies of $Cu_2O$ micro/nanocrystals and properties of CO self-sustained catalytic combustion

Pandong Ma [a,b], Zihao Teng [a], Qinglan Hao [a], Running Kang [b,c], Bei Li [a], Feng Bin [b,c,*], Baojuan Dou [a,*]

[a] College of Marine & Environmental Sciences, Tianjin University of Science & Technology, Tianjin 300457, PR China
[b] State Key Laboratory of High-Temperature Gas Dynamics, Institute of Mechanics, Chinese Academy of Sciences, Beijing 100190, PR China
[c] School of Engineering Science, University of Chinese Academy of Sciences, Beijing 100049, PR China

ARTICLE INFO

*Keywords:*
$Cu_2O$ micro/nanocrystals
Precursor concentration
Morphology
CO oxidation
Self-sustained catalytic combustion

ABSTRACT

The self-sustained catalytic combustion is one of the most effective ways to remove high concentration CO at low temperature. In this paper, $Cu_2O$ micro/nanocrystals with different morphologies were successfully synthesized by changing the precursor concentration using liquid phase reduction method. The obtained $Cu_2O$ were characterized using SEM, XRD, XPS, $H_2$-TPR and $O_2$-TPD, and the relationship between the catalytic performance and morphology was analyzed based on CO-TPD-MS and activity evaluation results. It was found that high precursor concentration leads to more exposure of active crystal planes of $Cu_2O$. Compared with $Cu_2O$-1 exposing only (1 0 0) crystal planes, $Cu_2O$-5, the precursor concentration of which is 5 times of $Cu_2O$-1, exposes (1 0 0) and (1 1 0) crystal planes. $Cu_2O$-9, with 9 times of precursor concentration of $Cu_2O$-1, exposes (1 0 0), (1 1 0) and (1 1 1) crystal planes simultaneously. All the obtained $Cu_2O$ with different precursor concentrations can achieve self-sustained CO catalytic combustion, and the catalytic activity increases with increasing precursor concentration ($Cu_2O$-1 < $Cu_2O$-5 < $Cu_2O$-9). The results prove that unsaturated coordination of Cu and O on the (1 1 1) and (1 1 0) planes can enhance the corresponding reducibility, adsorption and activation of gaseous oxygen, consequently promoting the CO oxidation to $CO_2$ over $Cu_2O$-9.

## 1. Introduction

A large amount of converter exhaust gas (CO ≤ 35%, $O_2$ ≥ 2%) produced in the process of steel-making with industrial converter which does not meet the recovery standard, is often discharged into atmosphere by methane combustion in the exhaust tower. The released gas accounts for about 20% of the total gas volume and consumes 1.3 million $m^3$ of $CH_4$ per year, leading to serious energy waste and environmental pollution. According to the characteristics of discharged gas, such as intermittent, periodic, great fluctuation of concentration and flow, self-sustained catalytic combustion technology has been adopted by our research group to achieve efficient removal of high concentration of CO at low temperature in the released gas. CO can maintain the sustainable combustion on the catalyst surface with complete conversion when the heat released from the reaction itself is greater than the heat emission of the reactor. The CO combustion over the catalyst is flameless, and the risk of explosion caused by flame propagation can be avoided. Furthermore, the heat from CO self-sustained catalytic combustion can be recovered. Therefore, the self-sustained catalytic combustion has become a highly competitive technology for CO removal with industrial application potential, owing to the advantages of high conversion rate and energy utilization rate, low initial investment and high economic benefit [1–4].

The catalyst is the key factor for the self-sustained catalytic combustion technology [1,5]. Our previous results of in situ infrared experiments confirmed that Cu (I) is the main site for CO adsorption in the process of CO oxidation on Cu based catalysts [3]. $Cu_2O$ micro/nanocrystalline possesses a large number of binding sites for CO adsorption due to the exposure of Cu (I) providing 4s1 empty orbit on its surface [6]. Hua et al. [7] found that the distribution and arrangement of atoms on the different $Cu_2O$ crystal plane are also different, which plays an important role in the catalytic activity. Zhang et al. [8] further found that the contribution of the crystal plane exposed at the surface, edge and corner positions in the CO catalytic oxidation varies with the

* Corresponding authors at: State Key Laboratory of High-Temperature Gas Dynamics, Institute of Mechanics, Chinese Academy of Sciences, Beijing 100190, PR China (F. Bin).
*E-mail addresses:* binfeng@imech.ac.cn (F. Bin), bjdou@tust.edu.cn (B. Dou).

https://doi.org/10.1016/j.fuel.2020.119776
Received 3 September 2020; Received in revised form 11 November 2020; Accepted 12 November 2020
Available online 9 December 2020
0016-2361/© 2020 Elsevier Ltd. All rights reserved.

particle size of $Cu_2O$ crystals. $Cu_2O$ micro/nanocrystal can be synthesized by many methods, including solid phase method, liquid phase method [9–11] and electroreduction method [12]. Among them, the liquid phase reduction method is widely used because of the regular morphology, uniform particle size, high crystallinity and good dispersion of $Cu_2O$. The process of preparing $Cu_2O$ by liquid-phase reduction method can be simplified as follows. Precipitant is added into Cu (II) solution at a specific temperature to precipitate Cu (II) in the form of Cu $(OH)_2$. After a period of reaction, a weak reducing agent is added to reduce $Cu(OH)_2$ to $Cu_2O$ [9]. In this process, the different concentration of precursor in the reaction system may influence the morphology, crystal structure, surface chemical properties and catalytic performance of $Cu_2O$ [13]. However, there is no relevant literature report on this aspect.

In this study, $Cu_2O$-1, $Cu_2O$-5 and $Cu_2O$-9 catalysts were prepared by controlling the precursor concentration with liquid phase reduction method. The activities of the catalysts were investigated by CO self-sustained catalytic combustion. SEM, XRD, XPS, $H_2$-TPR, $O_2$-TPD and CO-TPD-MS were used to characterize and analyze the morphology, crystal structure, chemical states, reduction ability and oxygen species. Furthermore, reaction pathways on the different planes of $Cu_2O$ were proposed. This study will provide experimental data for the self-sustained catalytic combustion technology to control the converter exhaust gas.

## 2. Experimental section

### 2.1. Catalyst preparation

The $CuCl_2{\cdot}2H_2O$, NaOH and ascorbic acid were obtained from Sinopharm Chemical Reagent Co. (China). All reagents as analytical grade were used directly without further purification, and an ultrapure water (18.25 MΩ) was used throughout the study. The procedure for the preparation of $Cu_2O$ micro/nanocrystals is illustrated in Fig. 1. $CuCl_2{\cdot}2H_2O$ (1.7 g, 0.01 mol) was first dissolved in 1.2 L ultrapure water (18.25 MΩ). After stirring the resulted solution for 30 min at 55 °C, NaOH (8.0 g, 0.2 mol) and ascorbic acid (10.6 g, 0.06 mol) was added into the solution, and the addition of both is as 30 min intervals. Then the mixture was stirred for 5 h at 55 °C. The brick-red color solid precipitate was gradually formed in the liquid phase reaction system. When the reaction was finished, the precipitates were washed with ultrapure water until the solution was neutral, and then were dried in vacuum at 60 °C for 12 h to prepare fresh $Cu_2O$-1 micro/nanocrystals [7]. $Cu_2O$ micro/nanocrystals prepared under different precursor concentrations are represented by $Cu_2O$-x, where x is the precursor concentration. With increasing the addition of $CuCl_2{\cdot}2H_2O$, NaOH and ascorbic acid to 5 times and 9 times, the obtained catalysts were recorded as $Cu_2O$-5 and $Cu_2O$-9, respectively.

### 2.2. Characterization

The morphology of catalysts was observed with a field-emission scanning electron microscope (SEM, Hitachi S4800) at the accelerating voltage of 30 kV. X-ray powder diffraction (XRD) measurements were performed with a Rigaku D/MAC/max 2500 v/pc diffractometer using the Cu Kα radiations ($\lambda = 1.54059$ Å) (X-ray tube was operated at 40 kV and 40 mA) in the $2\theta$ range at room temperature with a scanning step size of 0.02°. XRD data were analyzed by the HighScore Plus program to identify XRD patterns according to JCPDS data base. The chemical state and surface components of the catalysts was analyzed by X-ray photoelectron spectroscopy (XPS) on a Perkin-Elmer PHI-1600 using Mg Kα excitation. The reference binding energy was chosen to match the C1s binding energy of electrons in alkyl group equal to 284.8 eV with the accuracy of the peak position at 0.2 eV. Temperature programmed reduction of hydrogen ($H_2$-TPR) and temperature programmed desorption of oxygen ($O_2$-TPD) were carried out on a TP5080B chemisorption analyzer. With respect to $H_2$-TPR, each sample (15 mg) was first treated at 300 °C for 30 min in $N_2$ and cooled to room temperature in the same atmosphere, then swept with 5% $H_2$/Ar mixture (30 mL/min) until the base line on the recorder remained unchanged. Finally, the sample was heated at a rate of 10 °C/min to record the TPR spectra. For $O_2$-TPD, each sample (50 mg) was heated in a $N_2$ flow of 30 mL/min and maintained at 300 °C for 30 min. After that, an $O_2$ flow of 30 mL/min was switched to purge the sample for 30 min. Finally, the $O_2$-TPD experiment was carried out at a heating rate of 15 °C/min. The temperature-programmed desorption of CO (CO-TPD-MS) was performed on the same apparatus as that in $H_2$-TPR and $O_2$-TPD, coupling with a quadrupole mass spectrometer (Pfeiffer PrismaPlus). High purity CO was adsorbed on the sample for 30 min at room temperature and then was exposed to $N_2$. After the baseline was stable, the reactor was heated at a rate of 10 °C/min until reaching 600 °C and the TPD spectra were taken with the mass spectrometer.

### 2.3. Catalytic activity test

The catalytic activity was evaluated in a flow-type apparatus designed for continuous operation (Fig. 2). Specifically, about 50 mg of fresh catalyst, mixed with quartz sand as the same weight of catalysts, was packed into a quartz tube reactor with an inner diameter of 6 mm, an outer diameter of 8 mm and pretreated in a high purity $N_2$ atmosphere at 300 °C for 1 h to blow impurities before switching to the gas mixture. The length of catalyst bed was about 7 mm. During each temperature programmed oxidation (TPO) run, the heating/cooling rate was set at 5 °C/min. A constant feed composition was used, 10% CO, 21% $O_2$, with 69% $N_2$ balance, with a space velocity of 60,000 $h^{-1}$. The flow rates (0.2 L/min) were controlled by mass flow controllers with a full-scale measurement accuracy of ±1%. An online gas measurement system was employed to monitor the effluent CO, $O_2$ and $CO_2$ (QGS-08C for $CO/CO_2$ and BJYX-YX-306B for $O_2$, Maihak). The conversion rates of CO was obtained by the average of three experiments and calculated based on the concentrations of inlet and outlet gas. A K-type thermocouple (0.5 mm thick) was inserted near the catalyst bed to monitor the furnace temperature along the gas flow direction. After the CO conversion reaches 100%, the electric furnace can be removed in the experimental system. Then the temperature distributions on the reactor surface around the catalyst bed was acquired by an infrared camera

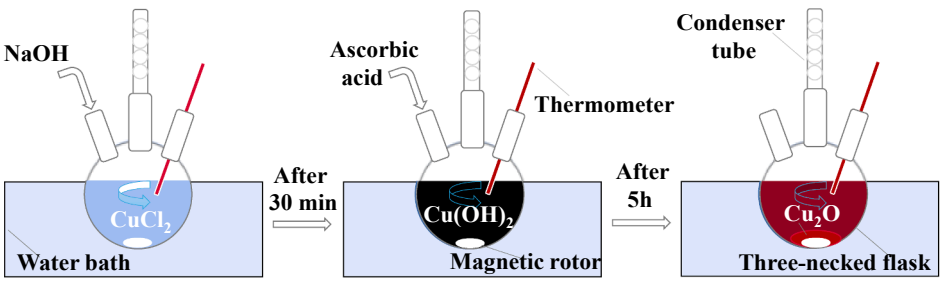


**Fig. 1.** Schematic illustration for the preparation process of $Cu_2O$ micro/nanocrystals.

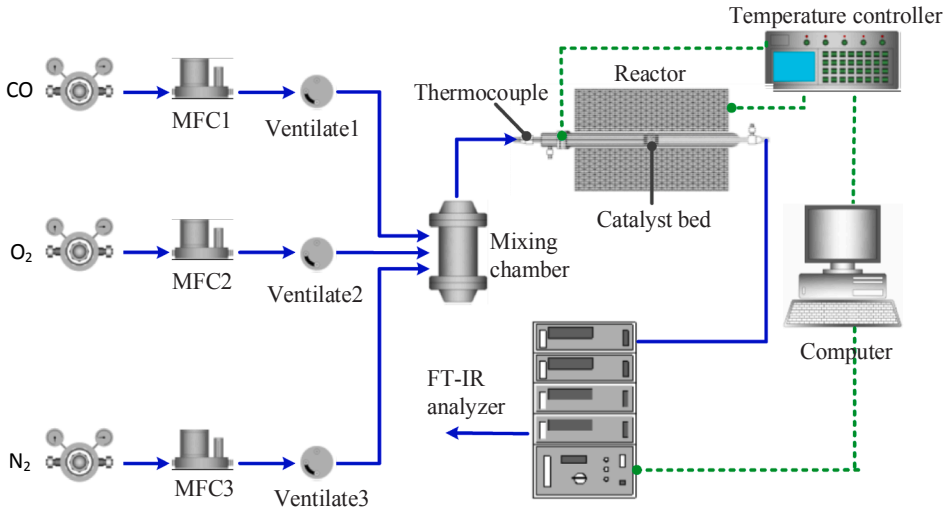


**Fig. 2.** Schematic diagram of the experimental set-up for CO self-sustained combustion (adapted from Ref. [4]).

(FLIR T640) with a measurement accuracy of ±2%.

### 2.4. Calculation of activation energy

The activation energy ($E_a$) of CO oxidation reaction was calculated by kinetic experiments on the activity evaluation device. The amount of catalyst and the composition of reaction gas were the same as those of activity evaluation. The catalyst was heated to the desired reaction temperatures at a rate of 5 °C/min and then kept there for 30 min until the catalytic reaction reached a steady state. The conversion of CO was calculated as

$$X_{CO} = \frac{[CO]_{in}\% - [CO]_{out}\%}{[CO]_{in}\%} \quad (1)$$

where $[CO]_{in}$ and $[CO]_{out}$ are the CO concentrations in the inlet and outlet gas, respectively. $X_{CO}$ was used to calculate the reaction rate via the following equation:

$$r_{CO} = \frac{N_{CO} \times X_{CO}}{W_{cat}} \quad (2)$$

where $N_{CO}$ is the CO molar gas flow rate in mol/s, $W_{cat}$ is the catalyst weight in grams, and $r_{CO}$ is the reaction rate in $mol_{CO}/(g_{cat}{\cdot}s)$.

$$k = A\exp\left(\frac{-E_a}{RT}\right) \quad (3)$$

$$\ln r_{CO} = \ln A - E_a/\mathrm{RT} \quad (4)$$

where $k$ is the reaction rate constant in $s^{-1}$, $A$ is the pre-exponential factors in $s^{-1}$, R is the molar gas constant in $kJ/(mol{\cdot}K)$, and $T$ is the reaction temperature in $K$. The $E_a$ can be evaluated from the slope of the plot $\ln r_{CO}$ versus 1000/T [3,13].

## 3. Results and discussion

### 3.1. CO self-sustained catalytic combustion

Fig. 3A shows the activity curves of CO self-sustained catalytic combustion over the $Cu_2O$-9, $Cu_2O$-5 and $Cu_2O$-1 catalysts, which can be roughly divided into three stages with the increase of temperature. The first stage exhibits a slow induction of CO conversion ≤5%, where reaction gases (CO + $O_2$) are adsorbed and activated on the catalyst surface, and then converted slowly into the $CO_2$ that is removed via the exhaust gas. The consumed reactants can be quickly replenished by internal diffusion. In this stage, the CO reaction rate is mainly controlled by the intrinsic reaction kinetics. The second stage can be ascribed as the transient light-off step (5% < CO conversion < 100%): with further increasing the temperature, the number of activated molecules in the reaction gas increases, leading to the CO conversion and reaction rate enhancing significantly. In this case, the chemical heat released by the oxidation of high concentration CO is greater than that of the reaction system. Then the actual temperature of the catalyst bed is not limited by

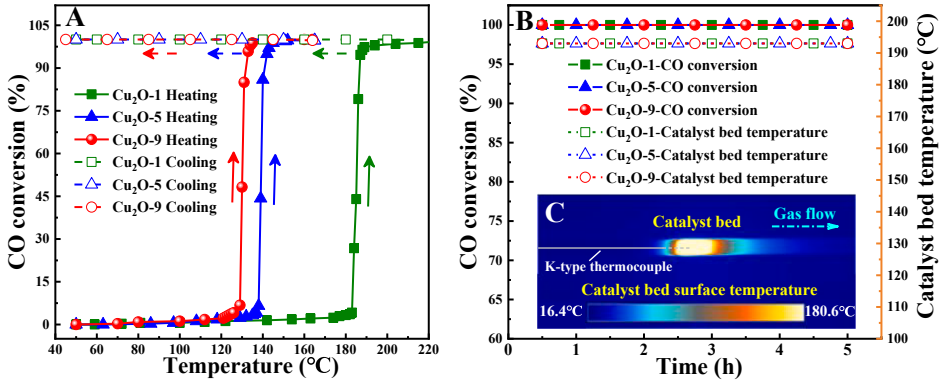


**Fig. 3.** Activity curves of CO self-sustained catalytic combustion (A), CO conversion and catalyst bed temperature within 5 h (B) over $Cu_2O$-9, $Cu_2O$-5 and $Cu_2O$-1 catalysts, and typical 2-D temperature field of the reactor outer surface during CO self-sustained combustion over $Cu_2O$-9 catalyst (C).

the temperature programmed. The instantaneous runaway reaches the ignition temperature of CO, resulting in CO spontaneously igniting on the catalyst surface. The conversion of CO is close to 100% at that time. Entering the third stage, the conversion is no longer affected by the temperature variation and the reaction mainly depends on the diffusion rate of reactants to the catalyst surface, external diffusion as well as catalyst activity. The $Cu_2O$-9 exhibits the highest low-temperature activity among all the catalysts tested according to the ignition temperatures $T_{50}$ of 130 °C (defined as the temperature at 50% CO conversion), followed by the $Cu_2O$-5 (138 °C) and then $Cu_2O$-1 (185 °C). The results obtained show that the CO oxidation activity of the catalysts increases with precursor concentration.

The $T_{50}$ of CO oxidation over different catalysts under different reaction conditions are summarized in Table 1. The ignition temperature of CO on Cu based catalysts is related to CO concentration and catalyst activity [1,4,14]. Compared with the catalysts prepared in the past [1,3], the activity of the $Cu_2O$ micro/nanocrystals catalyst is between $CuO/Ce_{0.75}Zr_{0.25}O_{2-\delta}$ and $Ce_{0.75}Zr_{0.25}O_{\delta}$. It can be explained by the fact that the activity of the $Cu_2O$ micro/nanocrystals mainly depends on the exposing crystal planes, and lack of highly dispersed CuO on the surface [3]. Compared with the noble metal catalysts (polycrystalline Pt, Rh) [15–18], the obtained $Cu_2O$ micro/nanocrystals exhibit relatively low $T_{50}$ under the specific experimental conditions.

Under the experimental conditions, once ignition occurs, even if the reactor temperature drops to room temperature, the conversion of CO can be maintained at 100% by using the chemical heat released from the CO oxidation reaction on the three catalysts. It can be seen from Fig. 3B that, within 5 h, the CO conversion is always maintained at 100%, and the maximum temperature of the catalyst bed center is 193 °C detected by a thermocouple wire in the center of the catalyst bed. Fig. 3C shows the two-dimensional temperature field distribution of CO self-sustaining combustion on $Cu_2O$-9 catalyst collected by an infrared camera (FLIR T640). The blue background is room temperature (16.4 °C). The temperature in the front and end of the catalyst bed is lower, and the temperature in the middle part is higher. The reason may be that the reaction gas at room temperature hardly reacts before reaching the front of the catalyst bed. After approaching the catalyst bed, the CO and $O_2$ are quickly adsorbed and activated on the catalyst surface, and then $CO_2$ is generated to desorb from the catalyst surface, leading to a large amount of chemical heat released, which makes the temperature in the middle of catalyst bed significant rise. Except for part of the heat generated used to maintain the continuous CO oxidation reaction, the rest of the heat is lost to the surrounding environment through heat transfer. However, there is not enough chemical heat to maintain the temperature at the end of catalyst bed because the CO in the gas phase has been completely converted into $CO_2$ along the pipe. Moreover, due to heat and mass transfer, the exhaust gas takes away part of the heat, resulting in the decrease of the temperature at the end of the catalyst bed.

**Table 1**
The ignition temperature ($T_{50}$) of CO oxidation over different catalysts under different reaction conditions.

| Samples | Reaction gas mixture | GHSV ($h^{-1}$) | $T_{50}$ (°C) | Reference |
|---|---|---|---|---|
| $CuO/Ce_{0.75}Zr_{0.25}O_{2-\delta}$ | 1% CO + 1%$O_2$/$N_2$ | 60,000 | 127 | [3] |
| $Cu_2O$-9 | 10% CO + 21%$O_2$/$N_2$ | 60,000 | 130 | This work |
| $Cu_2O$-5 | 10% CO + 21%$O_2$/$N_2$ | 60,000 | 138 | This work |
| $Cu_{0.07}Ce_{0.75}Zr_{0.25}O_{2-\delta}$ | 1% CO + 1%$O_2$/$N_2$ | 60,000 | 175 | [3] |
| $Cu_2O$-1 | 10% CO + 21%$O_2$/$N_2$ | 60,000 | 185 | This work |
| CuCe-Z | 5% CO + 20%$O_2$/$N_2$ | 30,000 | 189 | [1] |
| CuCe-Z | 3% CO + 20%$O_2$/$N_2$ | 30,000 | 198 | [1] |
| Cu-Z | 5% CO + 20%$O_2$/$N_2$ | 30,000 | 227 | [1] |
| CuCe-Z | 1% CO + 20%$O_2$/$N_2$ | 30,000 | 235 | [1] |
| Polycrystalline Pt | 6.1% CO + 30.2% $O_2$/$N_2$ | 120,000 | 237 | [17] |
| Polycrystalline Pt | 14% CO + 27.7% $O_2$/$N_2$ | 120,000 | 267 | [17] |
| Polycrystalline Rh | 14.2% CO + 30.9% $O_2$/$N_2$ | 120,000 | 267 | [18] |
| $Ce_{0.75}Zr_{0.25}O_{\delta}$ | 1% CO + 1%$O_2$/$N_2$ | 60,000 | 290 | [3] |

The $E_a$ value calculated by Arrhenius equation usually indicates the difficulty of the reaction of reactants on the catalyst [3]. The lower $E_a$ of CO oxidation reaction on the catalyst results in the easier reaction occurs, and the better activity of the corresponding catalyst [8]. Fig. 4 presents the Arrhenius plots of the CO reaction rates in the kinetic region over the $Cu_2O$-1, $Cu_2O$-5 and $Cu_2O$-9 catalysts. The activation energies ($E_a$) of CO oxidation for these catalysts are calculated as 84 ± 2 ($Cu_2O$-9), 92 ± 1 ($Cu_2O$-5) and 103 ± 2 kJ/mol ($Cu_2O$-1), which are similar to the range of activation energies previously reported for CO oxidation over CuO/o-$Cu_2O$ (73.4 ± 2.6 kJ/mol), CuO/c-$Cu_2O$-34 (82.3 ± 4.2 kJ/mol) and CuO/c-$Cu_2O$-1029 (118.5 ± 3.1 kJ/mol) catalysts [8,13]. These activation energies of CO oxidation reveal that the catalytic activities follow the order of $Cu_2O$-9 > $Cu_2O$-5 > $Cu_2O$-1, which is consistent with the results of the activity evaluation.

### 3.2. Morphology and structure

The morphologies of $Cu_2O$-1, $Cu_2O$-5 and $Cu_2O$-9 were clarified by SEM, as shown in Fig. 5. It can be seen from Fig. 5A that $Cu_2O$-1 is cubic exposing six (100) crystal planes [19–21]. When the precursor concentration increases to 5 times of $Cu_2O$-1 (Fig. 5B), the morphology of $Cu_2O$-5 is developed to polyhedron with six (100) and twelve (110) crystal planes [22]. With further increase of precursor concentration to 9 times of $Cu_2O$-1 (Fig. 5C), $Cu_2O$-9 exhibits polyhedron with six (100), twelve (110) and eight (111) crystal planes [10]. Consequently, the precursor concentration in preparation process influences the morphology evolution of $Cu_2O$ micro/nanocrystals significantly. It is suggested that changing the precursor concentration is an effective method to control the morphology of $Cu_2O$ micro/nanocrystals.

Fig. 6 shows the XRD patterns of $Cu_2O$-1, $Cu_2O$-5, $Cu_2O$-9, $Cu_2O$-9-u and $Cu_2O$-9-$H_2$-TPR. The diffraction peaks of $Cu_2O$ micro/nanocrystals appearing at 29.57°, 36.42°, 42.31°, 62.46°, 73.52° and 77.37°correspond to (110), (111), (200), (211), (311) and (222) of standard cubic phase of $Cu_2O$ (JCPDS No. 99-0041) [13,23], respectively, and no other diffraction peak of impurity is found. The intensity and sharpness of the diffraction peak increase with increasing precursor concentration, indicating a continuous enhancement of the crystallinity of $Cu_2O$. After activity evaluation, the diffraction peaks of $Cu_2O$-9-u at 36.42°, 62.46° and 73.52° are attributed to the (111), (211) and (311) crystal planes of cubic $Cu_2O$ (JCPDS card No. 99-0041), and the peaks at 35.40° and 38.96° are ascribed to (002) and (200) crystal planes of CuO (JCPDS card No. 45-0937) [20,21,24]. The appearance of CuO in $Cu_2O$-

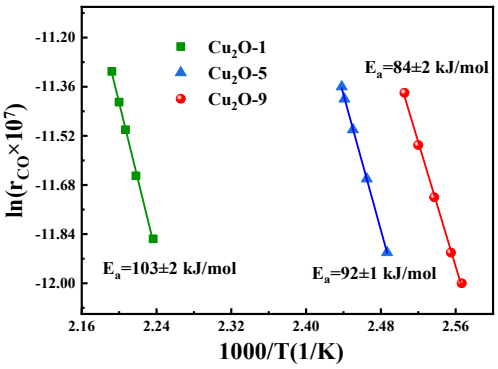


**Fig. 4.** Arrhenius plots for CO oxidation over $Cu_2O$-1, $Cu_2O$-5 and $Cu_2O$-9 catalysts.

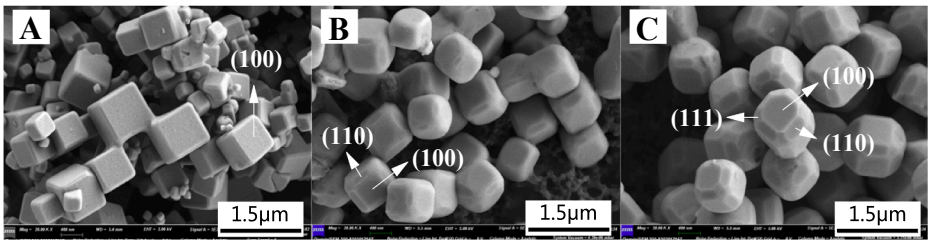


**Fig. 5.** SEM images of $Cu_2O$-1 (A), $Cu_2O$-5 (B) and $Cu_2O$-9 (C).

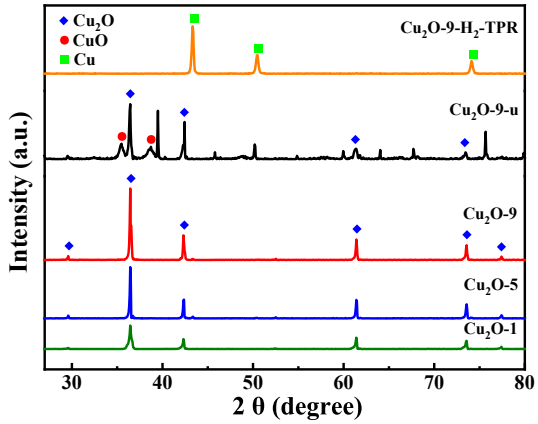


**Fig. 6.** XRD patterns of $Cu_2O$-1, $Cu_2O$-5, $Cu_2O$-9, $Cu_2O$-9-u ($Cu_2O$-9 after activity evaluation) and $Cu_2O$-9-$H_2$-TPR ($Cu_2O$-9 after $H_2$-TPR).

9-u can be explained by the proportion of $O_2$ in mixed reaction gas for the CO catalytic activity testing, which is excessive compared with the stoichiometric ratio of CO oxidation (see experimental section). Generally, Cu (I) catalysts are unstable and can be oxidized to Cu (II) [13]. And the $Cu_2O$ surface can be gradually oxidized to CuO during the temperature programmed process. The unlabeled diffraction peaks of $Cu_2O$-9-u belong to the diffraction peaks of quartz sand ($SiO_2$) doped in the catalyst. After $H_2$ reduction, the peaks at 43.32°, 50.45° and 74.12° of $Cu_2O$-9-$H_2$-TPR are attributed to the (111), (200) and (220) crystal planes of cubic Cu (JCPDS card No. 85-1326) [23,24], and no other diffraction peaks of impurities are found, indicating that all the Cu elements in $Cu_2O$-9-$H_2$-TPR exist in the form of metal Cu.

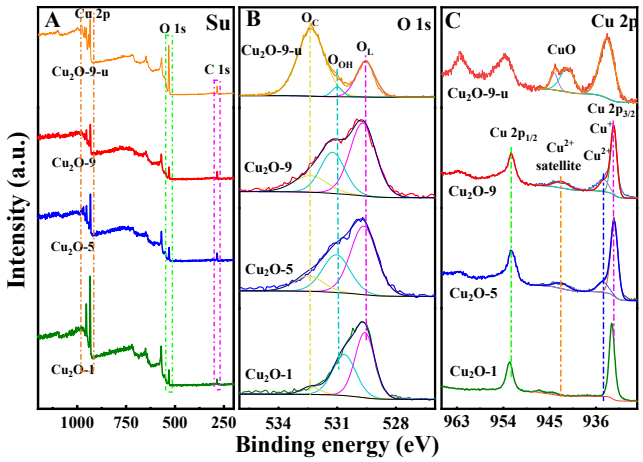


**Fig. 7.** XPS patterns of Su (A), O 1s (B) and Cu 2p (C) for the $Cu_2O$-1, $Cu_2O$-5, $Cu_2O$-9 and $Cu_2O$-9-u catalysts.

### 3.3. Chemical states

Fig. 7 shows the XPS spectra of Su, O 1s and Cu 2p for $Cu_2O$-1, $Cu_2O$-5, $Cu_2O$-9 and $Cu_2O$-9-u, and the corresponding surface atomic ratios are summarized in Table 2. It can be seen from Fig. 7A that the binding energies at 962 ~ 928, 535 ~ 526 and 284.8 eV are attributed to Cu 2p, O1s and C1s, respectively [3,26]. The relative intensity of Cu 2p peak decreases in the order of $Cu_2O$-1 > $Cu_2O$-5 > $Cu_2O$-9, indicating that the relative content of Cu species on the catalyst surface decreases with the increasing precursor concentration. After activity evaluation, the intensity of O 1s peak in $Cu_2O$-9-u is significantly enhanced, suggesting the increase of oxygen species on the catalyst surface.

As shown in Fig. 7B, the binding energy at 532.5 eV, 530.7 eV and 529.5 eV can be attributed to chemically adsorbed oxygen ($O_C$), hydroxyl oxygen ($O_{OH}$) and lattice oxygen ($O_L$), respectively [3,25,26]. As seen in Table 2, the relative content of surface $O_C$ in the three fresh catalysts decreases in the order of $Cu_2O$-9 (24.0%) > $Cu_2O$-5 (21.4%) > $Cu_2O$-1 (11.7%). After activity evaluation, the oxygen species on the $Cu_2O$-9-u surface are mostly in the form of $O_C$, and the relative content of $O_L$ reduces to 24.8%.

Fig. 7C shows that, with increasing precursor concentration, the half peak width of Cu (I) $2p_{1/2}$ and Cu (I) $2p_{3/2}$ at the binding energy of 952.7 eV and 932.7 eV gradually widens with greater asymmetry [25,26]. For $Cu_2O$-5 and $Cu_2O$-9, satellite peaks in the range of 938 ~ 942 eV and 960 ~ 963 eV attributed to Cu (II) are observed [23]. By fitting the peaks of Cu (I) $2P_{3/2}$, it is found that the Cu 2p spectra of $Cu_2O$-5 and $Cu_2O$-9 contain Cu (II) peaks attributed to $Cu(OH)_2$ [23] and Cu(I) peaks attributed to $Cu_2O$ [13], while $Cu_2O$-1 consist of only $Cu_2O$. This phenomenon can be explained by the fact that the alkalinity of the precursor increases with the concentration, and the same proportion of ascorbic acid cannot reduce all $Cu(OH)_2$ to $Cu_2O$, leaving a small amount of $Cu(OH)_2$ in the $Cu_2O$. Table 2 shows that the contents of Cu $(OH)_2$ in $Cu_2O$-1, $Cu_2O$-5 and $Cu_2O$-9 are 0, 17.4% and 20.6%, respectively, demonstrating that the enhanced basicity of the precursor is the main reason for the morphology evolution of $Cu_2O$ micro/nanocrystals. Only Cu (II) belonging to CuO is discovered in the XPS spectra of Cu 2p for $Cu_2O$-9-u, owing to the residual $Cu(OH)_2$ in the catalyst which decomposes into CuO and $H_2O$ with the increasing temperature [23,26]. On the other hand, the amount of $O_2$ in the reaction gas is excessive compared with the stoichiometric ratio of CO oxidation reaction, and the catalyst surface tends to be oxidized into CuO [13]. Therefore, the Cu species on $Cu_2O$ surface after activity evaluation mainly exists in the form of CuO. However, the XRD results show that a large amount of $Cu_2O$ still exists in $Cu_2O$-9-u, which verifies that only surface $Cu_2O$ is

**Table 2**
Surface atomic ratios of catalysts obtained by XPS quantitative analysis.

| Catalyst | Cu/O (%) | $O_C$/O (%) | $O_L$/O (%) | Cu(II)/Cu (%) |
|---|---|---|---|---|
| *$Cu_2O$-9-u | 29.1 | 72.1 | 24.8 | 100 |
| $Cu_2O$-9 | 69.0 | 24.0 | 50.1 | 20.6 |
| $Cu_2O$-5 | 77.1 | 21.4 | 49.4 | 17.4 |
| $Cu_2O$-1 | 138.0 | 11.7 | 50.5 | 0 |

*$Cu_2O$-9-u is $Cu_2O$-9 after activity evaluation.

oxidized during the CO catalytic reaction [8,13].

### 3.4. Reducibility and oxygen species

The $H_2$-TPR profiles of $Cu_2O$-1, $Cu_2O$-5, $Cu_2O$-9 and $Cu_2O$-9-Oxi catalysts are shown in Fig. 8. As shown in Fig. 8, the $H_2$-TPR profile of the $Cu_2O$-9 catalyst is characterized by three partially overlapping peaks at 195° C (α peak), 226 °C (β peak) and 290 °C (γ peak), which are lower than that of the $Cu_2O$-5, centered at 235 °C (β peak), 305 °C (γ peak) and 360 °C (δ peak). Only one reduction peak, labeled at 288 °C (γ peak) for $Cu_2O$-1 and 255 °C for $Cu_2O$-9-Oxi, can be observed, respectively. Based on the SEM results, $Cu_2O$-1 exposes only (1 0 0) crystal planes, while $Cu_2O$-5 exposes both (1 0 0) and (1 1 0) crystal planes, and $Cu_2O$-9 exposes (1 0 0), (1 1 0) as well as (1 1 1) crystal planes at the same time, which thus confirms that the reducibility of different catalysts is related to the exposure of typical crystal planes. As such, the α, β and γ peaks can be assigned to the reduction of (1 1 1), (1 1 0) and (1 0 0) crystal planes, respectively.

The central temperature and $H_2$ consumption of α, β and γ peaks are shown in Table 3. According to the ratio of different peaks $H_2$ consumption to total $H_2$ consumption, combined with the crystal planes exposure of catalysts, the contribution of different crystal planes in different catalysts to catalyst reducibility was obtained. Hence with respect to $Cu_2O$-1, the contribution of (1 0 0) crystal planes to reducibility is 100%; as for $Cu_2O$-5, the contribution of (1 1 0) to reducibility is 69%, and that of (1 0 0) is 23%; for the $Cu_2O$-9, the contribution of (1 1 1) to reducibility is 8%, that of (1 1 0) is 69%, and that of (1 0 0) is 23%. The experimental results are in a good agreement with the exposure ratio of crystal planes in SEM characterization. Combined with activity test results discussed above, the reducibility and activity of the three catalysts follow the order of $Cu_2O$-9 > $Cu_2O$-5 > $Cu_2O$-1, corresponding to the reducibility order of different crystal planes: (1 1 1) > (1 1 0) > (1 0 0). To verify the effect of CuO on the reducibility of catalysts, the reducibility of $Cu_2O$-9-Oxi is tested after the $Cu_2O$-9 was oxidized in air at 300 °C for 30 min, with the results indicating that the reduction temperature shifting toward high temperature direction compared with the $Cu_2O$-9. It can be speculated that the CuO phase presents to be inactive to the CO oxidation.

$O_2$-TPD is used to investigate the oxygen species in all catalysts. As shown in Fig. 9, all the catalysts display desorption peaks < 100 °C, assigned to the desorption of physisorbed oxygen ($O_P$, α peak). The $Cu_2O$-5 and $Cu_2O$-9 exhibit a desorption peak (β peak) attributed to surface chemically adsorbed oxygen ($O_C$) centered at 550 °C and 580 °C respectively, while no β peak is observed in the $O_2$-TPD profile of $Cu_2O$-1. Therefore, the adsorption capacity of catalysts follows the order of $Cu_2O$-9 > $Cu_2O$-5 > $Cu_2O$-1, which can be related to exposed crystal plane of the catalyst. The (1 1 1) and (1 1 0) planes exposed by $Cu_2O$-9

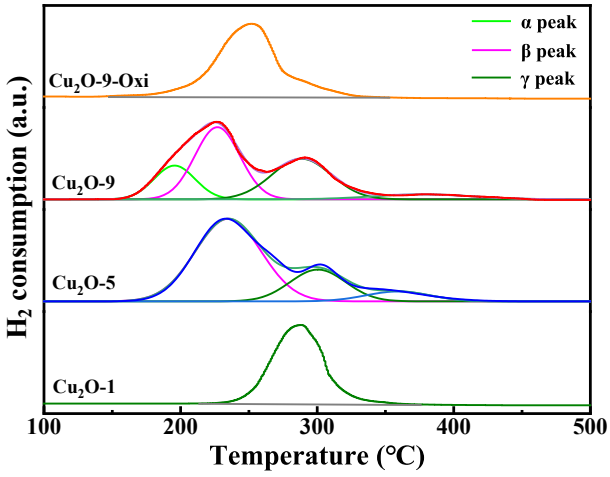


**Fig. 8.** $H_2$-TPR profiles of the $Cu_2O$-1, $Cu_2O$-5, $Cu_2O$-9 and $Cu_2O$-9-Oxi catalysts.

**Table 3**
$H_2$ consumption of the $Cu_2O$-1, $Cu_2O$-5, $Cu_2O$-9 and $Cu_2O$-9-Oxi catalysts.

| Catalyst | Temperature (°C) | | | $H_2$ consumption (mmol/g) | | | |
|---|---|---|---|---|---|---|---|
| | α peak | β peak | γ peak | α peak | β peak | γ peak | Total |
| *$Cu_2O$-9-Oxi | – | 255 | – | – | 4.66 | – | 4.66 |
| $Cu_2O$-9 | 195 | 226 | 290 | 0.35 | 2.95 | 0.96 | 4.26 |
| $Cu_2O$-5 | – | 235 | 305 | – | 3.05 | 0.99 | 4.40 |
| $Cu_2O$-1 | – | – | 288 | – | – | 4.49 | 4.49 |

*$Cu_2O$-9-Oxi is the catalyst for oxidation of $Cu_2O$-9 at 300 °C for 30 min in air.

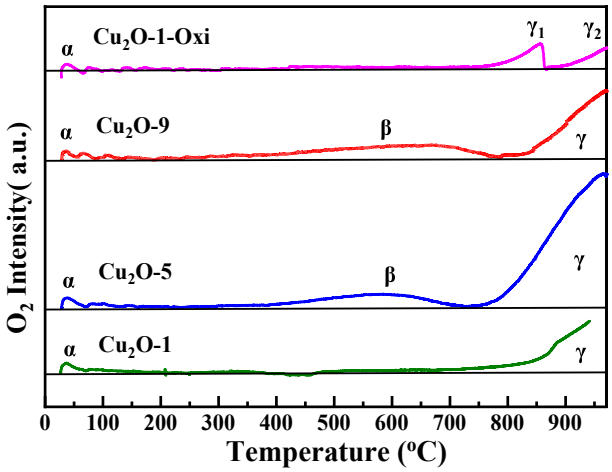


**Fig. 9.** $O_2$-TPD profiles of the $Cu_2O$-1, $Cu_2O$-5, $Cu_2O$-9 and $Cu_2O$-1-Oxi catalysts.

and (1 1 0) crystal planes exposed by $Cu_2O$-5 have many coordination unsaturated Cu atoms and strong adsorption capacity for $O_2$. At the high temperature range > 600 °C, the desorption peaks (γ peaks) attributed to lattice oxygen. The oxygen species on the catalyst surface is crossed, because the chemisorbed oxygen and lattice oxygen on the surface of transition metal oxides can be transformed into each other, and thus it is difficult to distinguish them strictly. To qualitatively verify the attribution of β and γ peak, the $Cu_2O$-1-Oxi is oxidized at 300 °C for 30 min under air condition before $O_2$-TPD. The $O_2$-TPD profile of $Cu_2O$-1-Oxi presents no desorption peak in the β peak temperature range (300 ~ 780 °C), but two desorption peaks ($\gamma_1$ and $\gamma_2$) belonging to lattice oxygen appear in the temperature range of γ peak. It is verified that $O_2$ can be hardly adsorbed on the surface of $Cu_2O$-1, and the β and γ peaks are attributed to the desorption of $O_C$ and $O_L$.

According to the semi quantitative results of $O_2$ desorption peak in Table 4, the contribution of different oxygen species to the $O_2$ desorption is as follows. With respect to $Cu_2O$-1, the contribution of $O_C$ to $O_2$ desorption is almost 0, and that of $O_L$ to $O_2$ desorption is 90%; As for $Cu_2O$-5, the contribution of $O_C$ to $O_2$ desorption is 15%, and that of $O_L$ to $O_2$ desorption is 82%; For $Cu_2O$-9, the contribution of $O_C$ to $O_2$ desorption is 32%, and that of $O_L$ to $O_2$ desorption is 61%, respectively. As expected, the $O_C$ with high ratio, which can be related to the strong

**Table 4**
$O_2$ consumption on the $Cu_2O$-1, $Cu_2O$-5, $Cu_2O$-9 and $Cu_2O$-1-Oxi catalysts.

| $O_2$ desorption (μmol·g$^{-1}$) | | | | |
|---|---|---|---|---|
| Catalyst | α peak | β peak | γ peak | Total |
| *$Cu_2O$-1-Oxi | 153 | – | 396 | 549 |
| $Cu_2O$-9 | 116 | 579 | 1099 | 1794 |
| $Cu_2O$-5 | 87 | 505 | 2720 | 3312 |
| $Cu_2O$-1 | 80 | – | 708 | 788 |

*$Cu_2O$-1-Oxi is the catalyst for oxidation of $Cu_2O$-1 at 300 °C for 30 min in air.

adsorption capacity of $O_2$, is beneficial to promote the adsorption and activation of gaseous oxygen on the catalyst surface, thus accelerating the CO oxidation reaction. Also as shown in Fig. 9, the contribution of $O_C$ to the $O_2$ desorption follows the order: $Cu_2O$-9 (32%) > $Cu_2O$-5 (15%) > $Cu_2O$-1 (0). This result indicates that the $O_2$ adsorption capacity of $Cu_2O$-9 and $Cu_2O$-5 is significantly higher than that of $Cu_2O$-1, which can be attributed to the effect of exposed crystal planes. As such, the $O_2$ adsorption capacity of different crystal planes decreases in the order of (1 1 1) > (1 1 0) > (1 0 0).

### 3.5. CO-TPD-MS analysis of catalysts

In heterogeneous catalysis, both the surface structure of catalysts and molecule surface adsorptions play an important role in the catalytic performance. In this study, CO-TPD-MS is applied to detect the CO adsorption on the $Cu_2O$-x catalysts, where the $CO_2$ as the only desorption product tracked by mass spectrometry in the tail gas. According to the $CO_2$ desorption peak and the corresponding desorption temperature, the CO-TPD-MS profiles of $Cu_2O$-9 and $Cu_2O$-5 catalysts (Fig. 10) can be divided into α and β peak, respectively. The catalytic activity for CO oxidation is mainly related to the low temperature desorption peak of $CO_2$ (α peak), and also consistent with the order of catalyst activity and reducibility detected from CO-TPO and $H_2$-TPR. For the $Cu_2O$-9, the initial temperature of α peak is 120 °C, which is 40 °C lower than that of α peak of $Cu_2O$-5 (160 °C), and 140 °C lower than that of β peak of $Cu_2O$-1 (260 °C). Combined with the results of SEM characterization and the paper published by Hua et al [7], the ideal surface structures of (1 1 1), (1 1 0) and (1 0 0) crystal planes are as follows: (1 1 1) as the outermost layer of the crystal plane is composed of three coordination unsaturated O atoms, and the Cu atoms in the second layer account for 25% of the total Cu atoms in this layer; (1 1 0) crystal plane, the outermost layer of which is composed of two coordination saturated Cu atoms and three coordination unsaturated O atoms simultaneously; (1 0 0) the outermost layer of crystal plane is the termination surface of O atoms, which is composed of two coordination unsaturated O atoms. Due to the open surface structure of (1 1 1), the $Cu_2O$ (1 1 1) exhibits the excellent catalytic activity for CO oxidation because of its easy contact with foreign reactants. Hence the CO oxidation activity of the three crystal planes follows the order of (1 1 1) > (1 1 0) > (1 0 0). Compared with $Cu_2O$-1, the (1 1 0) crystal planes exposed by $Cu_2O$-5 improves the CO oxidation, and the (1 1 1) crystal planes exposed by $Cu_2O$-9 on the basis of $Cu_2O$-5 further enhances its catalytic activity.

### 3.6. Reaction pathway of CO oxidation

The CO-TPD-MS experiments in this study show that the CO adsorbed on the catalyst surface combines with the $O_L$ and the formation $CO_2$ is closely related to the CO oxidation activity of the catalysts, hence $O_L$ of $Cu_2O$ participated in the CO oxidation, indicating the possibility of Mars-van-Krevelen (MvK) mechanism. In the process of CO oxidation catalyzed by $Cu_2O$ micro/nanocrystals, the adsorption and dissociation of reaction gases ($O_2$ and CO) induced by different exposed crystal planes play a key role in the catalytic activity. However, according to the experimental results of $O_2$-TPD and CO-TPO, the activity of $O_L$ in different crystal planes decreases in the order of (1 1 1) > (1 1 0) > (1 0 0), and $O_C$ is more active than $O_L$. According to the $O_2$-TPD and XPS O1s results, the $O_2$ adsorption capacity of $Cu_2O$-9 and $Cu_2O$-5 is significantly higher than that of $Cu_2O$-1, in accordance with $O_2$ adsorption capacity of (1 1 1) > (1 1 0) > (1 0 0). Furthermore, based on the exposure of $Cu_2O$ crystal planes, the activation energy of CO oxidation reaction on (1 1 1) crystal plane is the lowest, followed by (1 1 0) and (1 0 0). Hence the enhancement of $O_2$ adsorption capacity on (1 1 1) and (1 1 0) promoted the CO oxidation activity. According to the DFT calculation and partial pressure experiment published by Zhang et al. [8], it is proved that CO follow the MvK mechanism on the (1 1 0) plane of $Cu_2O$, and the reaction between CO and the active oxygen species adsorbed and activated by catalyst surface are very facile and proceed very fast. Therefore, MvK mechanism can explain the behaviors of CO self-sustained catalytic combustion on $Cu_2O$ micro/nanocrystals with different morphologies. Based the above analysis, the reaction pathways of CO oxidation on different crystal planes of micro/nanocrystals are supposed to be different, as shown in Fig. 11. On the (1 0 0) crystal planes, the possible elementary reactions of CO oxidation are as follows:

$$Cu(I) + CO \rightarrow [Cu(I) - CO] \quad (5)$$

$$[Cu(I) - CO] + O_L \rightarrow CO_2 + O_V + Cu(I) \quad (6)$$

$$O_V + O_2 \rightarrow O_L + O_C \quad (7)$$

$$[Cu(I) - CO] + O_C \rightarrow CO_2 + Cu(I) \quad (8)$$

From Fig. 11, CO is adsorbed on Cu (I) site of the (1 0 0) crystal planes and reacts with $O_L$ to produce $CO_2$, which is then desorbed from the catalyst surface and produces an oxygen vacancy ($O_V$). After $O_2$ chemisorption on the catalyst surface, one oxygen atom fills the previous $O_V$ to form $O_L$, and the other oxygen atom ($O_C$) continues to react with CO to generate $CO_2$, thus completing the whole process of catalytic cycle.

It has been confirmed by $O_2$-TPD that the (1 1 1) and (1 1 0) crystal planes of $Cu_2O$ have stronger ability for $O_2$ adsorption and activation than that of (1 0 0). Therefore, the possible elementary reactions of CO oxidation on the (1 1 0) and (1 1 1) planes are supposed as follows:

$$O_V + O_2 \rightarrow O_L + O_C \quad (9)$$

$$Cu(I) + CO \rightarrow [Cu(I) - CO] \quad (10)$$

$$[Cu(I) - CO] + O_C \rightarrow CO_2 + Cu(I) \quad (11)$$

$$[Cu(I) - CO] + O_L \rightarrow CO_2 + O_V + Cu(I) \quad (12)$$

The reaction pathway of CO on (1 1 0) and (1 1 1) crystal planes is similar. That is, $O_2$ is first adsorbed on $O_V$ on the catalyst surface, and then the chemisorbed CO on Cu (I) sites reacts with O atom suspended outside to generate $CO_2$, which is subsequently desorbed from the catalyst surface. And the following reaction steps are the same as those on (1 0 0) crystal planes. Owing to the higher activity of $O_C$ than $O_L$ [8], the activation energy of $[Cu(I) - CO] + O_C \rightarrow CO_2 + Cu(I)$ is lower than that of $[Cu(I) - CO] + O_L \rightarrow CO_2 + O_V + Cu(I)$. Compared with (1 0 0), the (1 1 1) and (1 1 0) crystal planes of $Cu_2O$ can promote the adsorption and activation of gaseous $O_2$, consequently optimizing the pathways of CO oxidation reaction. This is believed to be the main reason for the increased activity of $Cu_2O$-9 exposed (1 1 1) and (1 1 0) crystal planes.

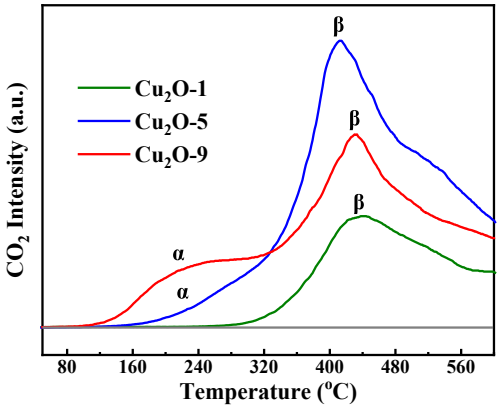


**Fig. 10.** CO-TPD-MS profiles of the $Cu_2O$-1, $Cu_2O$-5 and $Cu_2O$-9 catalysts.

## 4. Conclusions

The morphology of $Cu_2O$ micro/nanocrystals can be effectively controlled by simply changing the precursor concentration using the

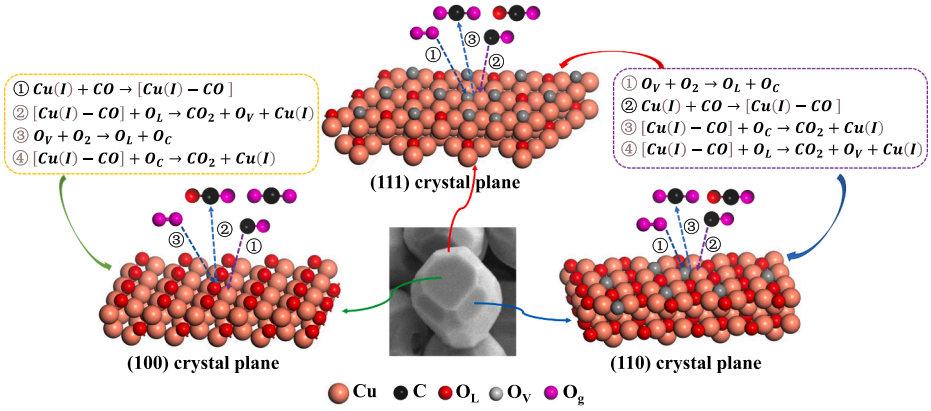


**Fig. 11.** The reaction pathways of CO oxidation over the (1 0 0), (1 1 0) and (1 1 1) crystal planes of $Cu_2O$.

liquid phase reduction method. And the increase of precursor concentration results in more exposure of active crystal plane of $Cu_2O$. $Cu_2O$-1 exposes only (1 0 0) crystal planes, while $Cu_2O$-5 exposes (1 0 0) and (1 1 0) crystal planes, and $Cu_2O$-9 exposes (1 0 0), (1 1 0) and (1 1 1) crystal planes simultaneously. The results further show that the CO self-sustained catalytic combustion is achieved on all the $Cu_2O$ micro/nanocrystals prepared with different precursor concentrations. The catalytic activity increases in the order of $Cu_2O$-1 < $Cu_2O$-5 < $Cu_2O$-9, indicating that the activity of CO oxidation is positively correlated with the low temperature reducibility of the catalyst. Compared with (1 0 0), some Cu and O coordination unsaturated on the (1 1 1) and (1 1 0) crystal planes enhance the ability to adsorb and activate the gaseous oxygen, thus promoting the oxidation of CO to $CO_2$ over $Cu_2O$-9. The obtained results provide experimental data for the CO self-sustained catalytic combustion technology and will benefit converter exhaust gas controlling.

## CRediT authorship contribution statement

**Pandong Ma:** Data curation, Writing - original draft, Writing - review & editing. **Zihao Teng:** Data curation, Validation. **Qinglan Hao:** Methodology, Supervision. **Running Kang:** Writing - review & editing. **Bei Li:** Software. **Feng Bin:** . **Baojuan Dou:** Writing - review & editing.

## Declaration of Competing Interest

The authors declare that they have no known competing financial interests or personal relationships that could have appeared to influence the work reported in this paper.

## Acknowledgments

We gratefully thank the financial support from the National Natural Science Foundation of China (No 51776216) and the Postdoctoral Science Foundation of China (No. 2017M623284).

## References

[1] Bin F, Wei X, Li B, Hui KS. Self-sustained combustion of carbon monoxide promoted by the Cu-Ce/ZSM-5 catalyst in $CO/O_2/N_2$ atmosphere. Appl Catal B 2015;162:282–8.
[2] Bin F, Kang R, Wei X, Hao Q, Dou B. Self-sustained combustion of carbon monoxide over $CuCe_{0.75}Zr_{0.25}O_\delta$ catalyst: Stability operation and reaction mechanism. Proc Combust Inst 2019;37(4):5507–15.
[3] Kang R, Wei X, Bin F, Wang Z, Hao Q, Dou B. Reaction mechanism and kinetics of CO oxidation over a $CuO/Ce_{0.75}Zr_{0.25}O_{2-\delta}$ catalyst. Appl Catal A 2018;565:46–58.
[4] Kang R, Wei X, Ma P, Bin F, He J, Hao Q, et al. Self-sustained combustion of CO with transient changes and reaction mechanism over $CuCe_{0.75}Zr_{0.25}O$ delta powder for honeycomb ceramic catalyst. Fuel 2020;263. https://doi.org/10.1088/2053-1591/ab6772.
[5] Bin F, Wei X, Li T, Liu D, Hao Q, Dou B. Self-sustained catalytic combustion of carbon monoxide ignited by dielectric barrier discharge. Proc Combust Inst 2017;36(3):4193–200.
[6] Jiang W, Ji W, Au CT. Surface/interfacial catalysis of (metal)/oxide system: structure and performance control. ChemCatChem 2018;10(10):2125–63. https://doi.org/10.1002/cctc.201701958.
[7] Hua Q, Cao T, Bao H, Jiang Z, Huang W. Crystal-plane-controlled surface chemistry and catalytic performance of surfactant-free $Cu_2O$ nanocrystals. ChemSusChem 2013;6(10):1966–72.
[8] Zhang Z, Wu H, Yu Z, Song R, Qian K, Chen X, et al. Site-resolved $Cu_2O$ catalysis in the oxidation of CO. Angew Chem Int Ed 2019;58(13):4276–80.
[9] Zhang DF, Zhang H, Guo L, Zheng K, Han XD, Zhang Z. Delicate control of crystallographic facet-oriented $Cu_2O$ nanocrystals and the correlated adsorption ability. J Mater Chem 2009;19(29):5220–5.
[10] Liang X, Gao L, Yang S, Sun J. Facile synthesis and shape evolution of single-crystal cuprous oxide. Adv Mater 2009;21(20):2068–71.
[11] Chang IC, Chen PC, Tsai MC, Chen TT, Yang MH, Chiu HT, et al. Large-scale synthesis of uniform $Cu_2O$ nanocubes with tunable sizes by in-situ nucleation. CrystEngComm 2013;15(13):2363–6.
[12] Hssi AA, Atourki L, Labchir N, Ouafi M, Abouabassi K, Elfanaoui A, Ihlal A, Bouabid K. Optical and dielectric properties of electrochemically deposited p-Cu2O films. Mater Res Express 2020;7(1): doi:10.1088/2053-1591/ab6772.
[13] Bao H, Zhang W, Hua Q, Jiang Z, Yang J, Huang W. Crystal-plane-controlled surface restructuring and catalytic performance of oxide nanocrystals. Angew Chem Int Ed 2011;50(51):12294–8.
[14] Kang R, Ma P, He J, Li H, Bin F, Wei X, et al. Transient behavior and reaction mechanism of CO catalytic ignition over a $CuO–CeO_2$ mixed oxide. Proc Combust Inst 2020. https://doi.org/10.1016/j.proci.2020.06.186.
[15] Deutschmann O, Schmidt R, Behrendt F, Warnat J. Numerical modeling of catalytic ignition. Symp (Int) Combust 1996;26(1):1747–54.
[16] Bär JN, Karakaya C, Deutschmann O. Catalytic ignition of light hydrocarbons over $Rh/Al_2O_3$ studied in a stagnation-point flow reactor. Proc Combust Inst 2013;34(2):2313–20.
[17] Zheng X, Mantzaras J, Bombach R. Kinetic interactions between hydrogen and carbon monoxide oxidation over platinum. Combust Flame 2014;161:332–46.
[18] Sui R, Mantzaras J, Bombach R. $H_2$ and CO heterogeneous kinetic coupling during combustion of $H_2/CO/O_2/N_2$ mixtures over rhodium. Combust Flame 2019;202:292–302.
[19] Hua Q, Cao T, Gu XK, Lu JQ, Jiang ZQ, Pan XR, et al. Crystal-plane-controlled selectivity of $Cu_2O$ catalysts in propylene oxidation with molecular oxygen. Angew Chem Int Ed 2014;53(19):4856–61.
[20] Park JC, Kim J, Kwon H, Song H. Gram-scale synthesis of $Cu_2O$ nanocubes and subsequent oxidation to CuO hollow nanostructures for lithium-ion battery anode materials. Adv Mater 2009;21(7):803–7.
[21] Kameyama N, Senna M. Effects of aging temperature on the size and morphology of $Cu(OH)_2$ and CuO nanoparticles. J Nanopart Res 2014;16(9):2584.
[22] Shang Y, Sun D, Shao Y, Zhang D, Guo L, Yang S. A facile top-down etching to create a $Cu_2O$ jagged polyhedron covered with numerous {110} edges and {111} corners with enhanced photocatalytic activity. Chem Eur J 2012;18(45):14261–6.
[23] Dan ZH, Lu JF, Li F, Qin FX, Chang H. Ethanol-mediated 2D growth of Cu2O nanoarchitectures on nanoporous Cu templates in anhydrous ethanol. Nanomaterials 2018;8(1):18.
[24] Feng L, Xuan Z, Bai Y, Zhao H, Li L, Chen Y, et al. Preparation of octahedral CuO micro/nanocrystals and electrochemical performance as anode for lithium-ion battery. J Alloy Compd 2014;600:162–7.
[25] Xu JF, Ji W, Shen ZX, Tang SH, Ye XR, et al. Preparation and characterization of CuO nanocrystals. J Solid State Chem 1999;147(2):516–9.
[26] da Rosa APP, Cavalcante RP, da Silva DA, da Silva LD, da Silva TF, Gozzi F, et al. $H_2O_2$-assisted photoelectrocatalytic degradation of Mitoxantrone using CuO nanostructured films: Identification of by-products and toxicity. Sci Total Environ 2019;651:2845–56.